

Particle Re-Suspension in Two-Phase Dispersed Rayleigh-Bénard Convection

Xianyang Chen,¹ Rodolfo Ostilla Monico,² Daniel Floryan,¹ and Andrea Prosperetti^{3,4,1,*}

¹*Department of Mechanical Engineering,*

University of Houston, Houston TX 77204, USA

²*Dpto. Ing. Mecánica y Diseño Industrial, Escuela Superior de Ingeniería,*

Universidad de Cádiz, 11519 Puerto Real, España

³*Faculty of Science and Technology, University of Twente,*

7500 AE Enschede, The Netherlands

⁴*Department of Mechanical Engineering,*

Johns Hopkins University, Baltimore MD 21218, USA

Abstract

The process by which particles are entrained by the fluid in Rayleigh-Bénard convection is studied by means of particle-resolved numerical simulations in a periodic domain at a Rayleigh number of 10^7 . The fluid Prandtl number is 1 and the particle-to-fluid density ratio 1.1. The results show that the horizontal velocity field near the bottom of the cell accumulates particles in heaps, or ‘dunes’, at the base of ascending plumes. The dunes deflect the incoming flow, conferring to it a vertical velocity component which entrains the particles up the dune and into the plume. An experimental observation of this mechanism was briefly reported by Solomatov *et al.* (*Earth Planet. Sc. Lett.* **120**, 387, 1993) but has not been considered further in the literature. By its very nature, such a process cannot be simulated by the point particle model. The final particle load carried by the convection depends both on the available gravitational energy of the fluid and on the effectiveness of the re-suspension mechanism.

I. INTRODUCTION

Rayleigh-Bénard natural convection with suspended particles is a situation encountered in a variety of settings such as air circulation in rooms and other built spaces [see, e.g., 1, 2], the ocean and the atmosphere [see, e.g., 3, 4], metal-production processes [see, e.g., 5] and magma chambers and other planetary processes [see, e.g., 6].

In Rayleigh-Bénard flow the fluid streamlines are, at least approximately, closed, and it might be thought that suspended particles could describe closed orbits remaining indefinitely entrained in the fluid circulation. The time-dependence and chaotic nature of the flow, however, confers to particles heavier than the fluid a non-zero probability of settling at the bottom of the convection cell so that all negatively buoyant particles might be expected to eventually settle. Experimental evidence does not conform with this expectation since it shows that it is possible for particles to be re-suspended in the convecting layer after deposition [see, e.g., 7, 8]. There is also indirect evidence from the geological record as continuous particle settling would be expected to produce a strong compositional differentiation, which is not always observed. Again, this fact suggests the presence of re-suspension processes [6, 9].

* aprosp@central.uh.edu

Several computational studies have examined the matter on the basis of Euler-Lagrange models with point particles [see, e.g., 10, 11]. By their very nature, these models cannot include a realistic account of re-suspension since, once particles are deposited on the bottom of the domain where the fluid velocity vanishes by the no-slip condition, there is no mechanism to re-suspend them in the convecting fluid. Park *et al.* [10] artificially re-injected settled particles in the fluid layer occupying the bottom 10% of their computational domain and found that sufficiently light particles could then be re-suspended even in a convective flow with a Rayleigh number as low as 2×10^6 , but the degree to which their procedure mimics the actual re-suspension mechanism is uncertain.

It appears that a necessary requirement for a computational approach to convincingly elucidate the re-suspension process is the ability to account for the particle finite size as done in the present paper. We simulate 500 particles in a standard three-dimensional Rayleigh-Bénard convection cell with periodicity conditions in the horizontal directions and a Rayleigh number of 10^7 . We also carry out simulations of up to 1000 particles in a quasi-two-dimensional domain, also with periodicity conditions in the horizontal directions. Our results are in qualitative agreement with the experimental observations reported by Solomatov *et al.* [8], who noticed that tangential stresses as considered in the Shields mechanism [see, e.g., 12] may be insufficient to entrain deposited particles. Rather, the circulating flow, which is nearly horizontal close to the cell bottom, causes the accumulation of the settled particles into structures that they refer to as ‘dunes’. These structures cause the bottom fluid velocity to acquire a component in the vertical direction, which is able to drag the particles upward, placing them in ascending fluid plumes.

II. MATHEMATICAL MODEL AND DIMENSIONLESS PARAMETERS

The fluid behavior is governed by the constant-properties Navier-Stokes equations in the Boussinesq approximation [see, e.g., 13]. The base of the computational domain is maintained at a temperature T_h and its upper surface at a temperature $T_c < T_h$. The fluid density is assumed to depend linearly on temperature according to $\rho(T) = \rho_0[1 - \beta(T - T_0)]$, in which $T_0 = \frac{1}{2}(T_h + T_c)$ and ρ_0 is the fluid density at $T = T_0$; β is the constant thermal

expansion coefficient. The Rayleigh Ra and Prandtl Pr numbers are defined by

$$Ra = \frac{g\beta(T_h - T_c)H^3}{\nu_f D_f} \quad \text{and} \quad Pr = \frac{\nu_f}{D_f}, \quad (1)$$

with $g = |\mathbf{g}|$ the acceleration of gravity, H the height of the cell and ν_f and D_f the fluid kinematic viscosity and thermal diffusivity.

Together with the cell aspect ratio, such a characterization would be sufficient for single-phase flow, but the presence of particles introduces several other important parameters. The single-particle Reynolds number Re_p is defined as $Re_p = d_p U_{term} / \nu_f$, in which d_p is the particle diameter and U_{term} the particle terminal velocity. Adopting for the drag coefficient the well-known Schiller-Naumann form [see, e.g., 14] $C_D = (24/Re_p)[1 + 0.15 Re_p^{0.687}]$, we find

$$U_{term} = \left(1 - \frac{\rho_0}{\rho_p}\right) g \tau_p \quad \text{with} \quad \tau_p = \frac{\rho_p d_p^2}{18 \rho_0 \nu_f (1 + 0.15 Re_p^{0.687})}, \quad (2)$$

the particle characteristic mechanical time [see e.g. 15]; ρ_p is the constant particle density. The mechanical Stokes number St (as opposed to the thermal Stokes number, introduced below) is defined by

$$St = \frac{\tau_p U_f}{H} \quad \text{with} \quad U_f = \sqrt{g\beta(T_h - T_c)H}, \quad (3)$$

the fluid free-fall velocity. Pertinent values of these and other particle parameters are listed in Table I.

The thermal Stokes number St_{th} , necessary to characterize the particle response time to temperature changes in its neighborhood, is defined by

$$St_{th} = \frac{\tau_{p,th} U_f}{H} \quad \text{with} \quad \tau_{p,th} = \frac{d_p^2 \rho_p c_{pp}}{6 k_f Nu_p}, \quad (4)$$

the particle thermal response time; here c_{pp} is the particle specific heat, k_f the fluid thermal conductivity and Nu_p the particle Nusselt number [see e.g. 10] estimated with the Ranz-Marshall correlation $Nu_p = 2 + 0.6 Pr^{1/3} Re_p^{1/2}$ [see, e.g., 14]. Note that this and the Schiller-Naumann correlations are only used to quantify the characteristic time scales of the particles. In the simulation the hydrodynamic force and the particle-fluid heat transfer are calculated from first principles.

We assume that the thermal diffusion time in a particle, of the order of $(d_p/2)^2/D_{p,th}$, with $D_{p,th}$ the particle thermal diffusivity, is smaller than $\tau_{p,th}$, which requires that $k_p/k_f > \frac{3}{2} Nu_p$,

with k_p the particle thermal conductivity. The value of Nu_p in the present simulations is 3.89. This inequality therefore is satisfied if the particle thermal conductivity is a bit more than an order of magnitude greater than that of the fluid. This assumption permits us to use the lumped capacitance approximation for the particles writing

$$m_p c_{pp} \frac{dT_p}{dt} = k_f \oint_{s_p} \nabla T \cdot \mathbf{n}_p ds_p, \quad (5)$$

in which \mathbf{n}_p is the outwardly directed unit normal at the particle surface s_p . Appendix B describes an estimate of particle-particle heat transfer upon collision and shows that this process is negligible in our conditions even when the particle thermal conductivity is large enough to justify the lumped capacitance approximation.

Several other dimensionless parameters are necessary to fully characterize our simulations. To the ones already listed, we may add the following ones

$$\frac{\rho_p}{\rho_0}, \quad \frac{c_{pp}}{c_{pf}}, \quad \frac{H}{d_p}, \quad \alpha = \frac{\pi}{6} \frac{d_p^3 N_p}{V}, \quad E_* = \frac{\nu_f^2 E}{\rho_0 (1 - \sigma^2) g^2 d_p^4}, \quad (6)$$

Here σ is the Poisson ratio, c_{pf} the constant fluid specific heat, α the particle volume fraction in the cell of volume V and E the Young modulus of the particle material that enters the collision model described in Appendix A. The parameter space is therefore considerably enlarged by the particles which renders a detailed investigation problematic. Another consequence of this large number of parameters is that it is next to impossible to isolate effects. For example, a change of ρ_p/ρ_0 would affect the particle Reynolds number Re_p and both Stokes numbers. A change to the mechanical Stokes number by changing H would cascade through several dimensionless groups. Adopting units such that $H = 1$ and $T_h - T_c = 1$, a common procedure in single-phase studies, would require to make specific choices for g and ν_f which would have major effects on Re_p and other parameters. These considerations have placed strong constraints on our choice of parameters that has been dictated by the selection of a small region of parameter space where we could expect some interesting results more than by the selection of a realizable physical system that could be investigated experimentally.

A related problem which is common in single-phase Rayleigh-Bénard convection but is seldom explicitly discussed in the literature is that the choice of parameters for which simulations are possible very often does not correspond to experimentally realizable situations. For example, for water at 20 °C with $T_h - T_c = 10$ K, $Ra = 10^7$, as in the present work,

would correspond to a cell with a height of only 41 mm. For air the cell height becomes 213 mm, but it is difficult to imagine solid particles with a density only 10% greater than air and, for this Rayleigh number, the convection is not strong enough to suspend much heavier particles. The ‘obvious’ solution would be to increase the Rayleigh number, but the Reynolds number of convection, on which particle suspension ultimately depends, is proportional to \sqrt{Ra} so that an increase by an order of magnitude would change things very little, while an increase by two orders of magnitude by increasing H would increase the total number of computational nodes by the same factor and place the resolved simulation of suspended particles completely outside the feasibility range. Increasing the Rayleigh number by increasing g or decreasing ν_f would increase the particle Reynolds number making them too heavy for suspension. These examples can easily be multiplied. The objective of this paper is to present one of the first resolved-particle simulations to begin the exploration of what happens when one leaves behind the point-particle models on which all the existing work on particulate Rayleigh-Bénard convection (save that of Kajishima and collaborators, see e.g. [16, 17], who simulated $Ra = 10^5$) has been invariably based until now.

Two cells were used in the simulations, in both cases with periodicity and no-slip boundary conditions applied on the vertical and horizontal faces, respectively. One cell was cubic, with aspect ratio 1 and a side $H = 20 d_p$. In this cell we ran simulations for about $180 H/U_f$ time units, preceded by $20 H/U_f$ time units as the flow was established. The computation lasted over two months on 8 Nvidia V-100 GPUs. The second cell was quasi-two dimensional, with height $H = 20 d_p$ and horizontal dimensions of $40 d_p \times 3 d_p$. Use of this latter cell was dictated by a desire to further study the re-suspension mechanism discovered in this work and to permit a (limited) exploration of the effect of particle number in a reasonable time.

We choose $d_p/2.5$ for the length scale and $(d_p/2.5)^2/\nu_f$ for the time scale. In these units the dimensionless free-fall velocity is $d_p U_f / (2.5 \nu_f) = \sqrt{4000} \simeq 63.25$. The temperature at the cell base is fixed at $T_h / (T_h - T_c) = +0.5$ and at the cell top at $T_c / (T_h - T_c) = -0.5$; furthermore $\beta(T_h - T_c) = 0.4$ and $(d_p/2.5)^3 g / \nu_f^2 = 200$.

ρ_p/ρ_0	Re_p	Nu_p	St	St_{th}	U_{term}/U_f	$\rho_p/\rho(T_c)$	$\rho_p/\rho(T_h)$	c_{pp}/c_{pf}
1.1	10.0	3.89	0.28	0.37	0.063	0.917	1.38	1

TABLE I. The value of some particle parameters used in the present simulations. The fluid parameters were held fixed: $Ra = 10^7$, $Pr = 1$, $\beta(T_h - T_c) = 0.4$.

III. NUMERICAL METHOD

The mathematical problem for the fluid is solved numerically by the PHYSALIS method, which has been thoroughly described in several earlier publications [see, e.g., 18, 19]. The method relies on the use of analytic general solutions for momentum and energy to replace boundary conditions on the particle surfaces by equivalent conditions on the neighboring nodes of a regular Cartesian grid. This procedure is made possible by the no-slip condition which, in the particle rest frame, makes the fluid velocity very small in the immediate neighborhood of the particle surface so that convection can be neglected. In the same very limited region (between the particle surface and the closest grid nodes) the time derivative of both velocity and temperature is also neglected so that the energy equation, for example, is approximated as $\nabla^2 T = 0$ and the momentum equations are approximated by the Stokes equations. These approximations, which are fully justified in the references cited, make analytical solutions available for the momentum and energy equations in the form of (suitably truncated) series of vector and scalar spherical harmonics multiplied by known functions of the distance from the particle center. For example, the solution of the energy equation in the immediate neighborhood of the particle surface is approximated as

$$T(\mathbf{x}, t) = T_p(t) + \sum_{\ell=0}^{\infty} \left[\left(\frac{r}{r_p} \right)^{\ell} - \left(\frac{r_p}{r} \right)^{\ell+1} \right] \sum_{m=-\ell}^{\ell} T_{\ell m}(t) Y_{\ell}^m(\theta, \phi), \quad (7)$$

in which Y_{ℓ}^m are spherical harmonics, $(r = |\mathbf{x}|, \theta, \phi)$ is a system of spherical coordinates centered at the particle center, r_p is the particle radius and the coefficients $T_{\ell m}(t)$ are chosen so as to match the solution of the complete unsteady convection-diffusion equation at the neighboring nodes. Similar expressions are available for the general solution of the Stokes equations [see, e.g., 20].

Since the coefficients multiplying the terms of the expansion (7) and the similar ones for velocity and pressure are unknown, the calculation proceeds by iteration. Starting with guessed values, a suitable truncation of the series is used to assign temperature, velocity

and pressure at the grid nodes closest to the particle surface. These values are used as boundary conditions to solve the (complete) Navier-Stokes and convection-diffusion equation throughout the fluid domain. New values of the coefficients are then obtained from these solutions by taking scalar products over surfaces concentric with the particles having a radius 15-20% greater than the particle radius. The difference between the coefficients obtained in this way and the previous values is used to drive the iterations. Convergence is ultimately achieved because, for a given set of boundary conditions, the field values on the scalar-product surface away from the particle surface are compatible with the boundary conditions only if the field equations are satisfied in the intervening layer. A very useful aspect of this approach is that the coefficients of the expansions embody important physical information such as the hydrodynamic force, hydrodynamic torque and heat transfer rate for each particle, thus avoiding the need to integrate the numerical result for the fluid stress and heat flux over the particle surface. For example, it is readily shown upon substituting the expansion (7) in (5) that

$$k_f \oint_{s_p} \nabla T \cdot \mathbf{n}_p ds_p = 2\sqrt{\pi}r_p k_f T_{00}(t). \quad (8)$$

Given the limited Reynolds number of the fluid-particle motion that we encounter in the present paper (see Table I), on the basis of grid convergence studies carried out in earlier works [18, 19, 21, 22], for the present simulations we have used uniform Cartesian grids with 8 nodes per particle radius. Again on the basis of past experience, the summations in the general solutions for the energy and momentum equations have been truncated to the first 16 and 46 terms, respectively.

Equation (B.3) of Appendix B gives the time t_c during which two colliding particles remain in contact. After non-dimensionalization this expression becomes

$$\frac{\nu_f t_c}{d_p^2} = 1.69 \left(\frac{5\pi}{1296} \right)^{2/5} \frac{1}{Re_{St}} \left[\frac{\rho_p}{\rho_f} \left(\frac{\rho_p}{\rho_f} - 1 \right)^2 \frac{1}{E_*} \right]^{2/5}, \quad (9)$$

in which $Re_{St} = \frac{1}{18}(\rho_p/\rho_f - 1)gd_p^3/\nu_f^2$ is the particle Reynolds number based on the Stokes velocity, (rather than the terminal velocity, which includes a Reynolds-number dependent correction that must be calculated numerically) and the dimensionless Young modulus E_* is defined in (6). In our simulations we use $E_* = 10^6$ which, for example for water, with $\sigma \simeq \frac{1}{2}$ and d_p between 1 and 0.1 mm, would correspond to E between 10^5 and 10^9 Pa. With this value the mechanical characteristic time τ_p is about 12 times the contact time and the time

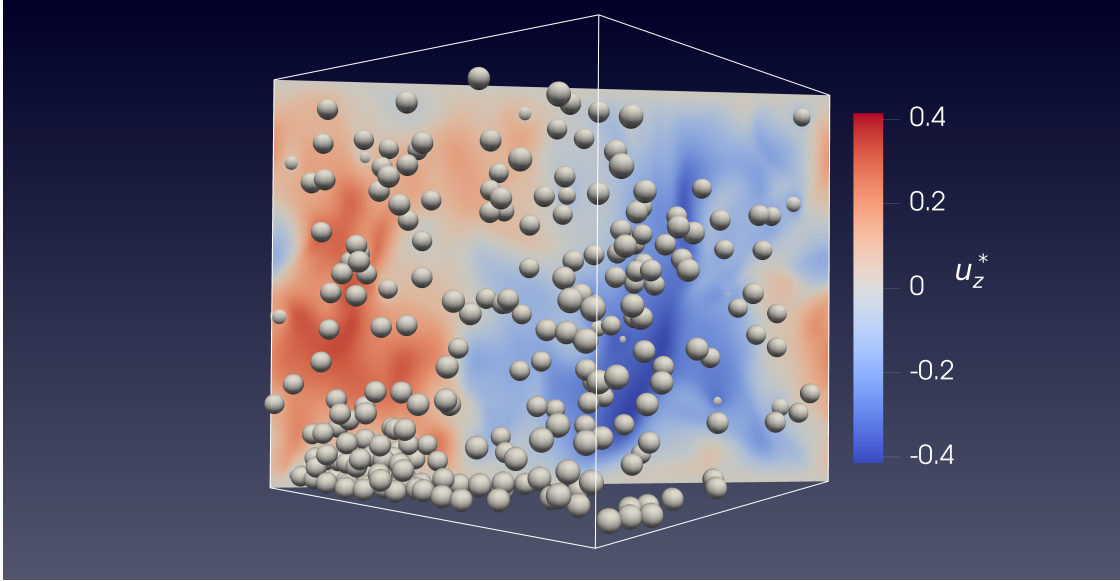


FIG. 1. Snapshot of a simulation with 500 particles with a density $\rho_p/\rho_0 = 1.1$ and an average volume fraction of 3.27%. The Rayleigh number is 10^7 and the Prandtl number is 1. The color on the plane cutting diagonally through the cell indicates the normalized vertical velocity $u_z^* = u_z/U_f$.

step used in the calculations about 23 times smaller. Collisions can therefore be resolved in the simulations.

IV. THE RE-SUSPENSION MECHANISM

At a Rayleigh number comparable to the one of our simulations, $Ra = 10^7$, the flow structure in single-phase Rayleigh-Bénard convection consists of buoyant plumes rising from the warm boundary layer at the bottom of the cell and cold plumes descending from the cold boundary layer forming along the cold top. These plumes drive a large-scale circulation, also known as mean wind, with a size of the order of the plate separation and a nearly vertical orientation [see e.g. 23]. In a doubly periodic domain, the plumes wiggle around but do not move very much. At our Rayleigh number the flow is mildly turbulent with a Reynolds number $HU_f/\nu_f \simeq 3200$. In the range $3 \times 10^8 \lesssim Ra \lesssim 10^{11}$ the effect of the Prandtl number for fixed Ra is less than 2% for $4 \lesssim Pr \lesssim 34$. Our simulations add $N_p = 500$ particles, achieving a mean volume fraction of 3.27%, but the character of the flow remains largely unchanged.

Figure 1 is a snapshot from a simulation in which $N_p = 500$ particles with a mean volume

fraction of 3.27% are suspended in a Rayleigh-Bénard flow with $Ra = 10^7$ and $Pr = 1$. Movie 1, showing the time development of this flow, is available at https://doi.org/***. In the figure the color on the vertical plane cutting diagonally through the cell is the fluid vertical velocity and shows ascending and descending plumes, in red and blue, respectively. In addition to the suspended particles, a point to note, which is the focus of this article, are the particles on the bottom of the cell and, in particular, the particles heaped up in a ‘dune’ in a corner of the domain.

The mechanism by which a dune is formed is illustrated in figure 2, which is a snapshot of the vertical velocity on a horizontal plane one diameter above the base of the cell. Blue and red colors correspond to negative (descending) and ascending fluid velocities, respectively. In the figure, arrows are attached to particles with a center within one particle diameter of the bottom and their length indicates the horizontal velocity of each particle. Near the bottom of the cell the fluid flow is approximately horizontal, with the rms of the vertical velocity on the plane of the figure about 2.6 times smaller than the horizontal velocity, and 5.6 times smaller on a horizontal plane located one particle radius below it. By continuity, this horizontal flow is directed from regions under the descending plume to regions under the ascending one which, at this time instant, forms a roughly cylindrical curtain encircling the descending plume. Particles that have settled on the bottom are exposed to this flow, which pushes them toward the base of the ascending plume where they accumulate. The drag imposed by the flow is sufficiently strong that particles form heaps as in figure 1.

To quantify the number of particles in dunes at any given time, we use a variant of the union-find algorithm based on the distance between the centers of particle pairs. A particle is declared to belong to a cluster when the distance of its surface from that of another particle belonging to the cluster is less than or equal to zero. Particles that are classified as bottom particles either belong to clusters (of whatever size) resting on the bottom, or are isolated particles touching the bottom. The black line in figure 3(a) shows, as a function of time, the total number of bottom particles while the red line is the number of particles in the largest dune. The simulations are started by keeping the particles fixed in random positions until the convection is established, at which point, taken as $t = 0$, they are released. The accumulation shows a temporary peak, still part of the initial transient, and eventually stabilizes fluctuating around a value of about 71 bottom with a standard deviation of 16. The average number of particles in the largest dune is 37 ± 16 .

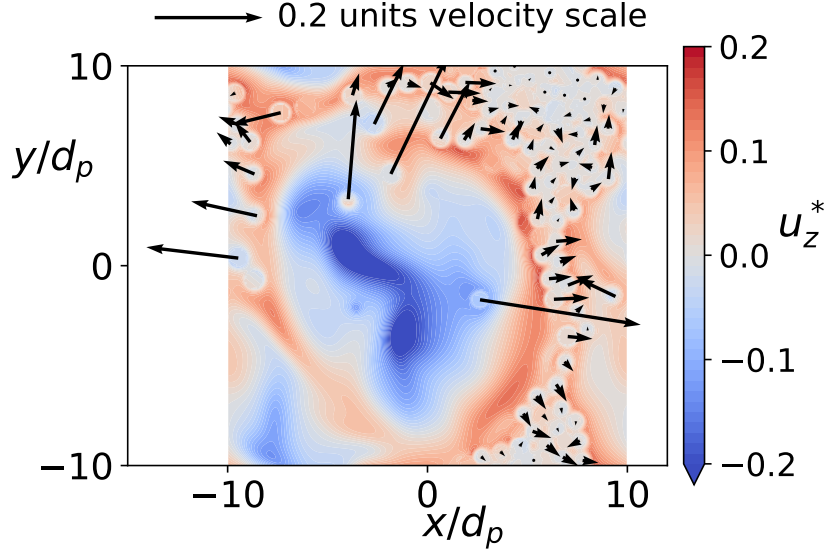


FIG. 2. The color is the normalized fluid vertical velocity $u_z^* = u_z/U_f$ on a horizontal plane one diameter above the cell base. The rms absolute value of the vertical velocity at this distance from the cell bottom is 2.6 times smaller than the horizontal velocity; one radius above the bottom it is 5.5 times smaller. Arrows indicate the horizontal velocity of particles with a center within one diameter of the base.

Figure 3(b) shows the joint probability density function of the normalized particle temperature and the normalized vertical position. The figure shows that the warmest particles are concentrated near the bottom of the cell. Most of these particles belong to the largest dune and help reinforce the ascending plume. Particles distributed throughout the height of the cell mostly have a temperature close to the average value $\frac{1}{2}(T_h + T_c)$. Near the bottom we see slightly cooler particles that have fallen from the colder region while the particles near the top are slightly warmer having been transported by the rising plume. The situation has some analogies with that described in Morize *et al.* [24], who studied particle re-suspension by thermal plumes in a Rayleigh-Bénard-type setup. Their cell, filled with a water-calcium chloride mixture, initially had a uniform particle layer at its bottom. At the beginning of the experiment, heating began to be applied over the central part of the cell bottom. When the liquid acquired sufficient buoyancy, a plume formed and was able to carry the particles upward.

The physics of the re-suspension process becomes clearer if we consider a quasi-two-dimensional cell with aspect ratio 2. The height is $20 d_p$ as before, but the dimensions of

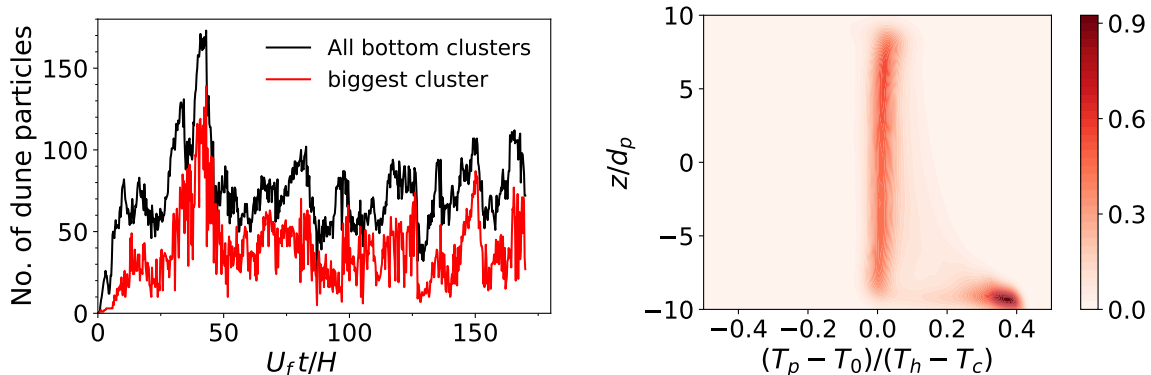


FIG. 3. (a) The red line shows the number of particles belonging to the largest bottom cluster (dune) vs. time. The black line is the total number of particles, clustered, or unclustered, on the cell bottom. Both lines refer to the simulation of figures 1 and 2. (b) Joint probability density function of the particle vertical position and normalized temperature.

the base are $40 d_p \times 3 d_p$. Doubling the length of the base has the effect of producing two counter-rotating convection cells, as shown in figure 4. The two cells form a dune by the same mechanism described in connection with figure 2. The mechanism by which the dune favors particle re-suspension is illustrated in figure 5 for $N_p = 150$ (left) and $N_p = 500$: the hollow circles show the positions of the black, blue and red particles at earlier times and trace out their trajectory as the particles fall to the cell bottom, are pushed toward the dune, dragged up its slopes and ultimately re-suspended into the ascending stream. Unlike the previous case, in this quasi-two-dimensional cell essentially all the bottom particles belong to a single large dune.

The average number of suspended particles, $N_{p,s}$, for the simulations with $N_p = 150, 300, 500$ and 1000 is given in Table II and, normalized by N_p , is shown in figure 6(a) vs. the average particle volume fraction ϕ ; the vertical bars are the standard deviations. The rapid increase of $N_{p,s}/N_p$ for the first three data points indicates that the number of suspended particles increases more than proportionally to the total number of particles. It must be concluded that the number of suspended particles is not only limited by the load-carrying capacity of the recirculating stream, but also by the rate at which particles can be re-suspended, with the efficacy of the re-suspension mechanism increasing with N_p . A possible explanation is the increase of the dune size with particle number shown in figure 5. For $N_p = 1000$, we find that the dune is largest (not shown, but see Movie 3 at

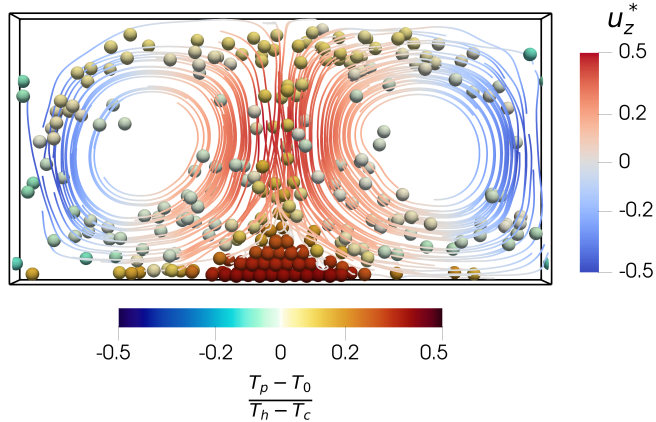


FIG. 4. Instantaneous streamlines and particle dune for the flow in a cell with aspect ratio 2, $Ra = 10^7$ and $Pr = 1$; the total number of particles is 300 and $\rho_p/\rho_0 = 1.1$. The dune has been placed at the center of the domain bottom by taking advantage of the lateral periodicity of the simulations. The streamlines are colored by the normalized vertical velocity $u_z^* = u_z/U_f$. Movie 2, available at https://doi.org/***, shows the time history of this simulation.

https://doi.org/***), but the fraction of suspended particles is approximately the same as for $N_p = 500$ (figure 6a). The flattening of the data for $N_{p,s}/N_p$ vs ϕ suggests a saturation of the load-carrying ability of the convection. The number of particles forming the dune, which is the counterpart of the number $N_{p,s}$ of suspended particles, is shown as a function of time in figure 6(b) for the simulations with 150, 300, 500 and 1000 particles. The system behavior for $N_p = 150, 300$ and 500 is very similar. For $N_p = 1000$ the particles initially slump to the cell bottom forming a continuous layer which, little by little is eroded forming a dune over a relatively long period of time.

V. ENERGETICS OF PARTICLE SUSPENSION

Table II shows the present computed results for several quantities of interest. The first two lines are the computed values for the time-averaged suspended particle number $N_{p,s}$ and corresponding particle volume fraction ϕ_s .

In their study, Solomatov and Stevenson [9] drew attention to E_f , the gravitational

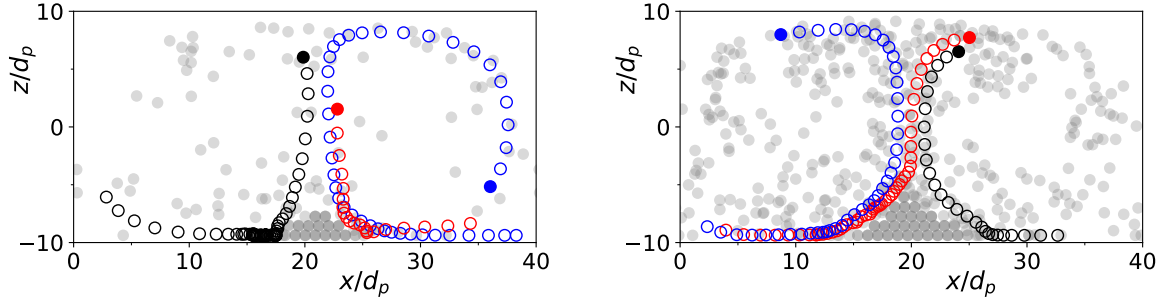


FIG. 5. (a) Illustration of the re-suspension mechanism for $N_p = 150$ (left) and $N_p = 500$. The hollow circles show the positions of the black, blue and red particles at earlier times. The particle dune imparts a vertical component to the fluid velocity which entrains particles into the ascending stream above the dune.

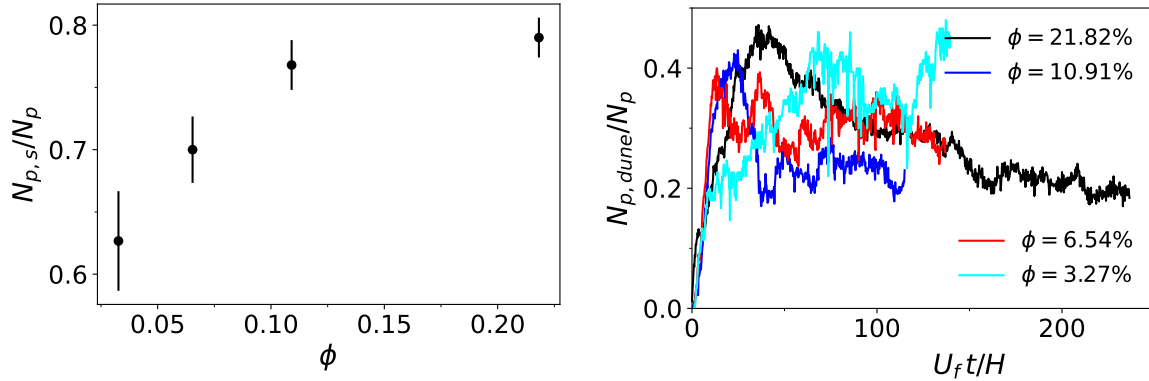


FIG. 6. (a) Fraction of suspended particles $N_{p,s}/N_p$ vs. the average particle volume fraction. (b) Number of particles $N_{p,d}$ forming a dune divided by the total number of particles N_p vs. normalized time in the quasi-two-dimensional simulations.

potential energy gained by the fluid per unit time, and the corresponding potential energy for the particles, E_p . We define these two quantities by

$$E_p = -v_p \mathbf{g} \cdot \overline{\sum_{\alpha=1}^{N_p} [\rho_p - \rho(T_p^\alpha)] \mathbf{U}_\alpha}, \quad E_f = -\beta \rho_0 \mathbf{g} \cdot \overline{\int_{V_f} (T - T_0) \mathbf{u} dV_f}, \quad (10)$$

in which the overline denotes the time average, $v_p = \frac{\pi}{6} d_p^3$ is the common particle volume, \mathbf{u} is the fluid velocity and T_p^α and \mathbf{U}_α the instantaneous temperature and velocity of the α -th particle. A consideration of the time-averaged fluid kinetic energy balance leads to the

	$N_p = 500$	$N_p = 150$	$N_p = 300$	$N_p = 500$	$N_p = 1000$
$N_{p,s}$	429 ± 16	94 ± 6	210 ± 8	384 ± 10	790 ± 16
ϕ_s	$(2.81 \pm 0.10)\%$	$(2.05 \pm 0.13)\%$	$(4.58 \pm 0.17)\%$	$(8.38 \pm 0.22)\%$	$(17.2 \pm 0.35)\%$
E_p	0.857×10^5	0.145×10^5	0.485×10^5	0.778×10^5	1.25×10^5
E_f	3.17×10^6	9.00×10^5	8.68×10^5	8.28×10^5	7.01×10^5
Φ	3.07×10^6	8.68×10^5	7.78×10^5	7.06×10^5	5.37×10^5
\dot{W}_{hd}	1.48×10^5	0.371×10^5	1.15×10^5	1.62×10^5	2.31×10^5
$\epsilon = E_p/E_f$	2.76%	1.61%	5.59%	9.40%	17.8%
Nu	17.39	16.5	16.43	16.33	15.6
E_p^{Sol}	3.09×10^5	0.676×10^5	1.50×10^5	2.74×10^5	5.58×10^5
ϵ^{Sol}	9.75%	7.51%	17.3%	33.1%	79.6%
$\tau_T/(\rho_p - \rho_0)gd_p$	0.099	0.096	0.091	0.086	0.076

TABLE II. Time-averaged computed results for various flow quantities defined in section V. The computed single-phase Nusselt numbers are 16.9 and 16.4 for the aspect-ratio 1 and 2 cells, respectively; $\tau_T = \sqrt{\mu_f \Phi / V}$ is the buoyancy stress scale defined in Solomatov *et al.* [8].

relation

$$\Phi \equiv \frac{1}{2\mu_f} \int_{V_f} \boldsymbol{\tau} : \boldsymbol{\tau} dV_f = E_f + E_p - \dot{W}_{hd} \quad \text{with} \quad \dot{W}_{hd} = \sum_{\alpha=1}^{N_p} \left(\overline{\mathbf{U}_\alpha \cdot \mathbf{f}_\alpha^{hd}} + \overline{\boldsymbol{\Omega}_\alpha \cdot \mathbf{l}_\alpha^{hd}} \right), \quad (11)$$

with $\boldsymbol{\tau}$ the viscous stress tensor and \dot{W}_{hd} the work per unit time performed by the hydrodynamic force \mathbf{f}_α^{hd} (without the buoyancy contribution) and couple \mathbf{l}_α^{hd} on the α -th particle translating with velocity \mathbf{U}_α and rotating with angular velocity $\boldsymbol{\Omega}_\alpha$. In single-phase convection $E_p = \dot{W}_{hd} = 0$ and one recovers the standard relation $E_f = \Phi$ in which the integrals are over the entire cell volume V rather than over V_f , the cell volume excluding the particles, as here. The quantities E_p , E_f , Φ and \dot{W}_{hd} , as well as E_p^{sol} defined in (12), are all scaled by $\rho_0 \nu_f^3 / (d_p / 2.5)$.

Solomatov and Stevenson [9] estimated E_f from the single-phase relation $E_f = \Phi$, an approximation that, in the light of the data in Table II, is not unreasonable. On the other hand, their estimate for E_p is

$$E_p^{Sol} \simeq \frac{\rho_p - \rho_0}{\rho_{av}} g M_{p,s} U_{term} = \frac{\rho_p}{\rho_{av}} \phi_s V (\rho_p - \rho_0) g U_{term}, \quad (12)$$

with $M_{p,s} = \frac{\pi}{6} d_p^3 N_{p,s} \rho_p$ the mass of suspended particles and $\rho_{av} = (1 - \phi)\rho_0 + \phi\rho_p$ the average mixture density. Aside from the factor ρ_p/ρ_{av} which, in our simulations, is not very different from 1, this relation is based on approximating the vertical component of the particle velocity \mathbf{U} in (10) by the terminal velocity. While particles may be at terminal velocity relative to the fluid parcel which surrounds them, it would seem that \mathbf{U} should include the velocity of the latter as well. The same point is made in Sturtz *et al.* [25]. The omitted term is not small since, from the fact that the average vertical particle velocity must vanish, it can be deduced that its average must be equal and opposite the terminal velocity. A comparison of E_p from (10) with E_p^{Sol} from (12) (with U_{term} from Table I), both calculated from the results of our simulations using for ϕ_s the volume fraction of the suspended particles only, is shown in Table II. As can be seen, the difference is in fact substantial, with E_p^{Sol} consistently greater than our E_p .

This difference acquires further importance if we turn to the ratio $\epsilon = E_p/E_f$ which Solomatov and Stevenson [9] introduced to quantify the efficiency with which the particles partake of the gravitational energy acquired by the fluid per unit time. Their estimate for this efficiency parameter gives it a small value, 0.6 - 0.9%. Table II shows ϵ as computed with our definitions of E_f and E_p and ϵ^{Sol} computed from $\epsilon^{Sol} = E_p^{Sol}/\Phi$. The first thing to notice is the substantially larger value of both our ϵ and ϵ^{Sol} in comparison with the estimate in Solomatov & Stevenson's paper. Secondly, ϵ^{Sol} is consistently greater than our computed value even approaching 80% for $N_p = 1000$. This value is so large as to reinforce the doubts expressed before on the way in which E_p^{Sol} is calculated.

In the paper in which they introduced the idea of dunes and their importance for re-suspension, Solomatov *et al.* [8] also concluded that re-suspension takes place when the parameter $\sqrt{\mu_f \Phi / V} / [(\rho_p - \rho_0) g d_p]$ is around 0.1. Our results for this quantity, also shown in Table II, are in good agreement with this estimate. The particles have a very modest effect on the cell Nusselt number, which is reduced by only about 5% by a particle volume fraction as high as 21.8%.

Lavorel and Le Bars [26] used the same estimate as E_p^{Sol} for the particle gravitational energy omitting the factor ρ_p/ρ_{av} . Upon using their Eq. (12) to calculate ϕ_s with the parameters of our simulations we find $\phi_s \sim O(0.1)\%$, an order of magnitude or more smaller than our computed values. Another somewhat related paper is the study by Sturtz *et al.* [25] which presents experimental results on the erosion of a particle-dense layer on the surface of

a volumetrically heated liquid. In this paper, however, velocities were of the order of mm/s and the particle-liquid density contrast was of the order of 10^{-3} . These parameters are so different from ours that no meaningful comparison seems possible.

The gravitational potential energy of particles suspended in Rayleigh-Bénard convection is ultimately dependent on the buoyant work done by gravity on the fluid and one might wonder why the efficiency estimated by Solomatov & Stevenson is so much smaller than the values that we have calculated. In commenting the fact that, in the experiments by Martin and Nokes [7] on which they based in part their considerations, the suspended solid fraction was surprisingly small, the authors say “it is more likely that ... [particle] reentrainment could not occur because the local mechanisms were not able to reentrain the particles, independently of our energetic criterion.” The results that we have described suggest that the missing ‘local mechanisms’ for re-suspension were dunes, which probably could not easily form in Martin & Nokes’s system due to the smallness of their particles relative to the boundary layer thickness on the cell bottom.

Intense vortices localized above a sand bed are also known to re-suspend particles [see e.g. 27], and this is indeed at the root of the Shields mechanism of particle transport in the flow of air or water over sand [see e.g. 12]. However, this mechanism relies on intense vorticity near the surface of the particle layer and would require a much larger Rayleigh number to be effective in Rayleigh-Bénard convection. At our Ra vortices are not localized but span the entire cell height. We have carried out some preliminary simulations with a single particle exposed to the same Rayleigh-Bénard flow and we have never observed a vortex-induced re-suspension process.

VI. CONCLUSIONS

The objective of this study was the elucidation, by computational means, of the mechanism by which particles subjected to Rayleigh-Bénard convection become re-suspended in the flow once they have fallen to the bottom of the cell. This phenomenon cannot be studied by relying on the widely-used point-particle model for the obvious reason that particles with zero volume resting on the no-slip bottom are not subjected to any flow. The only option is to carry out particle-resolved simulations, which we have done at a Rayleigh number of 10^7 . (It may be noted in passing that the only other simulations of this nature currently

available have been conducted for $Ra = 10^5$, see e.g. [17].)

We have found that the flow near the bottom of the cell, directed from the touch-down spot of the descending plume toward the base of the ascending plume, entrains the particles resting on the bottom leading to the formation of heaps, or ‘dunes’ (figures 2 and 5). Other particles are entrained up the sides of the dunes thus acquiring a vertical velocity component which, once they reach the top of the dune, facilitates their entrainment by the ascending flow. This re-suspension mechanism, therefore, is not dependent on lift, but on drag forces. Since dunes are fairly stable on the time scale of the fluid circulation, they heat up (figure 3b) and strengthen the ascending plumes, which favors the re-suspension process. This mechanism was first described in a short 1993 paper by Solomatov *et al.* reporting the results of an experiment with polystyrene spheres in water but has only been mentioned occasionally in the literature [see e.g. 6].

The ready formation of dunes is favored when particles are not deeply embedded inside the convection momentum boundary layer. In our simulations the ratio of the particle diameter d_p to the boundary-layer thickness δ (estimated using the wind-velocity, calculated as the average of the modulus of the vertical velocity on a plane at the cell mid-height) is $d_p/\delta \simeq 1.17$. The particles, therefore, are subjected to significant flow and the mechanism of dune formation of figure 2 can be quite effective. For much smaller values of d_p/δ re-suspension would be expected to be due to the Shields mechanism [see e.g. 12] which requires a much larger Rayleigh number to become effective in Rayleigh-Bénard convection.

In their study of particle suspension in natural convection, Solomatov and Stevenson [9] focused on the energetics of particle suspension predicting a very small rate of conversion of fluid to particle gravitational energy. The results that we find for this ratio are significantly greater than this estimate. Our explanation for the difference is that, in addition to the energetic cost of keeping particles in suspension, a crucial role is played by the effectiveness of the process by which particles are re-suspended, which Solomatov & Stevenson did not consider.

ACKNOWLEDGMENTS

The authors acknowledge the use of the Carya and Sabine clusters and are grateful to Dr. J. Ebalunode of the UH Research Computing Data Core for his support.

This study has been supported in part by the National Science Foundation Program CBET TTP under grant No. 2053204.

Appendix A: Collision modeling

Particle-particle and particle-boundary collisions are handled by a soft-particle contact-force model, which provides the forces and the couples on the colliding particles, described in detail in Sierakowski and Prosperetti [18]. The model is based on work of Tsuji *et al.* [28] and Barnocky and Davis [29]. The normal component of the collision force between two particles α and β is given by

$$\mathbf{F}_n = [-k_n(-h)^{3/2} - \eta_n(\mathbf{w}^\alpha - \mathbf{w}^\beta) \cdot \mathbf{n}] \mathbf{n}, \quad (\text{A.1})$$

in which \mathbf{n} is a unit vector directed from the center of particle β to that of particle α , $(-h)$ is the amount of overlap between two geometric spheres separated by the distance between the particle centers, k_n is given by

$$\frac{\sqrt{2}}{3} \frac{E \sqrt{r_p}}{1 - \sigma^2}, \quad (\text{A.2})$$

with σ the Poisson ratio, E Young's modulus, and η_n a damping parameter defined by

$$\eta_n = \alpha(e) \sqrt{\frac{1}{2} m_p k_n (-h)^{1/4}}. \quad (\text{A.3})$$

Here $\alpha(e)$ is a function of the coefficient of restitution e which can be approximated by [18]

$$\alpha(e) = 2.22 - 2.26 e^{0.4}. \quad (\text{A.4})$$

For the tangential force we start from the velocity of the point of contact \mathbf{s}

$$\frac{d\mathbf{s}}{dt} = (\mathbf{l} - \mathbf{nn}) \cdot \left[\mathbf{w}^\alpha - \mathbf{w}^\beta - \frac{1}{2}(2r_p + h)(\boldsymbol{\Omega}^\alpha - \boldsymbol{\Omega}^\beta) \times \mathbf{n} \right], \quad (\text{A.5})$$

with \mathbf{l} the identity two-tensor and $\boldsymbol{\Omega}$ the particle angular velocity. Then we calculate the elastic tangential force using

$$\mathbf{F}_t = \frac{ds}{dt} k_t, \quad (\text{A.6})$$

with the tangential stiffness k_t given by Mindlin's theory [30]

$$k_t = \frac{\sqrt{2} E}{(1 - \sigma^2)(1 + \sigma)} \sqrt{-r_p h}. \quad (\text{A.7})$$

To ensure that the tangential force coincides with the tangential plane we project it back onto the current tangential plane by $(\mathbf{l} - \mathbf{nn}) \cdot \mathbf{F}_t \rightarrow \mathbf{F}_t$. Should \mathbf{F}_t exceed that which can be supported by the frictional coefficient μ_f , $|\mathbf{F}_t| \leq \mu_f |\mathbf{F}_n|$, \mathbf{F}_t is set to $\mathbf{F}_t = \mu_f |\mathbf{F}_n| (\mathbf{F}_t / |\mathbf{F}_t|)$.

Appendix B: Particle-particle contact heat transfer

Particles do not exchange heat only with the fluid but also with other particles when they collide. This latter mode of energy transfer has been considered in Takeuchi *et al.* [17] and other studies from the same group in their simulations with $k_p/k_f = 100$ and $Ra = 10^5$.

Sun and Chen [31] have studied the average heat transfer coefficient upon particle collisions in a gas fluidized bed. Since, in their situation, the effect of the interstitial fluid is essentially absent, one may expect that their estimate is the result of more energetic collisions than in a liquid, resulting in a stronger deformation of the particles and therefore an increased heat transfer. On the other hand, the duration of the contact would be expected to be smaller, which would decrease the heat transfer. Davis *et al.* [32] considered the effect of the interstitial fluid and came up with the same scaling (B.3) as Sun & Chen up to constants of order one which will be seen to be unimportant for the matter of present concern.

For equal particles, Sun & Chen's Eq. (24) reduces to

$$h_c = 0.435C \frac{N_p v}{V} \rho_p c_{pp} A_c \sqrt{D_{p,th} t_c}, \quad (\text{B.1})$$

in which $C > 1$ is a coefficient of order 1, N_p the total number of particles in the domain of volume V , v the typical collision velocity, A_c the area of the contact disk and t_c the duration of the contact. For equal particles the area is given by

$$A_c = \pi \left(\frac{20\pi \rho_p r_p^5 (1 - \sigma^2)}{64E} \right)^{2/5} v^{4/5}, \quad (\text{B.2})$$

with σ the Poisson ratio and E Young's modulus, and the duration of the contact by

$$t_c = 3.38 \left(\frac{20\pi \rho_p r_p^3 (1 - \sigma^2)}{16E} \right)^{2/5} (r_p v)^{-1/5}. \quad (\text{B.3})$$

We take the Stokes terminal velocity $U_{St} = (\rho_p/\rho_f - 1)gd_p^2/(18\nu_f)$ as the characteristic collision velocity v , with the corresponding Reynolds number $Re_{St} = d_p U_{St}/\nu_f$ and find (9) for $\nu_f t_c/d_p^2$ and

$$\frac{A_c}{\pi r_p^2} = \left(\frac{5\pi}{5184} \frac{\rho_p}{\rho_f} \left(\frac{\rho_p}{\rho_f} - 1 \right)^2 \frac{1}{E_*} \right)^{2/5}. \quad (\text{B.4})$$

The Nusselt number for collision heat transfer can then be written as

$$Nu_c = \frac{d_p h_c}{k_f} = 0.738 \left(\frac{5\pi}{2592} \right)^{3/5} \frac{C\alpha}{E_*^{3/5}} \left(\frac{\rho_p}{\rho_f} \right)^{11/10} \left(\frac{\rho_p}{\rho_f} - 1 \right)^{6/5} \sqrt{Pr Re_{St} \frac{k_p c_{pp}}{k_f c_{pf}}}.$$

With the parameters of the simulations, $C = 1$ and $k_p/k_f = 1$ this relation gives $Nu_c \sim 0.0046$, about three orders of magnitude smaller than the value $Nu_p \sim 3.9$ of the Nusselt number for fluid-particle heat exchange of the present simulations (see Table I). In order to achieve a comparable Nusselt number it would be necessary that $k_p/k_f \sim 10^6$, very much larger than the particle conductivity necessary to justify the lumped-capacitance approximation (5).

-
- [1] S. Balachandar, S. Zaleski, A. Soldati, G. Ahmadi, and L. Bourouiba, Host-to-host airborne transmission as a multiphase flow problem for science-based social distance guidelines, *Int. J. Multiphase Flow* **132**, 103439 (2020).
 - [2] S. Rayegan, C. Shu, J. Berquist, J. Jeon, L. Zhou, L. Z. Wang, H. Mbareche, P. Tardif, and H. Ge, A review on indoor airborne transmission of COVID-19 - modelling and mitigation approaches, *J. Build. Eng.* **64**, 105599 (2023).
 - [3] A. F. Stein, R. R. Draxler, G. D. Rolph, B. J. B. Stunder, M. D. Cohen, and F. Ngan, NOAA's HYSPLIT atmospheric and dispersion modeling system, *Bull. Am. Meteorol. Soc.* **96**, 2059 (2015).
 - [4] H. S. Auta, C. U. Emenike, and S. H. Fauziah, Distribution and importance of microplastics in the marine environment: A review of the sources, fate, effects, and potential solutions, *Environ. Int.* **102**, 165 (2017).
 - [5] R. A. Jarvis and A. W. Woods, The nucleation, growth and settling of crystals from a turbulently convecting fluid, *J. Fluid Mech.* **273**, 83 (1994).
 - [6] L. Elkins-Tanton, Magma oceans in the inner solar system, *Annu. Rev. Earth Planet. Sci.* **40**, 113 (2012).
 - [7] D. Martin and R. Nokes, A fluid-dynamical study of crystal settling in convecting magmas, *J. Petrol.* **30**, 1471 (1989).
 - [8] V. Solomatov, P. Olson, and D. Stevenson, Entrainment from a bed of particles by thermal convection, *Earth Planet. Sci. Lett.* **120**, 387 (1993).
 - [9] V. S. Solomatov and D. J. Stevenson, Suspension in convective layers and style of differentiation of a terrestrial magma ocean, *J. Geophys. Res.: Planets* **98**, 5375 (1993).
 - [10] H. J. Park, K. O'Keefe, and D. H. Richter, Rayleigh-Bénard turbulence modified by two-way

- coupled inertial, nonisothermal particles, *Phys. Rev. Fluids* **3**, 034307 (2018).
- [11] V. Patočka, N. Tosi, and E. Calzavarini, Residence time of inertial particles in 3D thermal convection: implications for magma reservoirs, *Earth Planet. Sc. Lett.* **591**, 117622 (2022).
- [12] M. Ouriemi, P. Aussillous, M. Medale, Y. Peysson, and É. Guazzelli, Determination of the critical Shields number for particle erosion in laminar flow, *Phys. Fluids* **19**, 061706 (2007).
- [13] G. Ahlers, S. Grossmann, and D. Lohse, Heat transfer and large scale dynamics in turbulent Rayleigh-Bénard convection, *Revs. Modern Phys.* **81**, 503 (2009).
- [14] R. Clift, J. Grace, and M. Weber, *Bubbles, Drops, and Particles* (Academic Press, Cambridge, U.S.A., 1978) reprinted by Dover, 2013.
- [15] F. Lucci, A. Ferrante, and S. Elghobashi, Is Stokes number an appropriate indicator for turbulence modulation by particles of Taylor-length-scale size?, *Phys. Fluids* **23**, 025101 (2011).
- [16] J. Gu, S. Takeuchi, T. Fukada, and T. Kajishima, Vortical flow patterns by the cooperative effect of convective and conductive heat transfers in particle-dispersed natural convection, *Int. J. Heat Mass Transfer* **130**, 946 (2019).
- [17] S. Takeuchi, Y. Miyamori, J. C. Gu, and T. Kajishima, Flow reversals in particle-dispersed natural convection in a two-dimensional enclosed square domain, *Phys. Rev. Fluids* **4**, 084304 (2019).
- [18] A. Sierakowski and A. Prosperetti, Resolved-particle simulation by the Physalis method: Enhancements and new capabilities, *J. Comput. Phys.* **309**, 164 (2016).
- [19] Y. Wang, A. Sierakowski, and A. Prosperetti, Fully-resolved simulation of particulate flows with particles-fluid heat transfer, *J. Comput. Phys.* **3**, 638 (2017).
- [20] S. Kim and S. J. Karrila, *Microhydrodynamics: Principles and Selected Applications* (Butterworth-Heinemann, Boston, MA, 1991).
- [21] D. P. Willen, A. J. Sierakowski, G. Zhou, and A. Prosperetti, Continuity waves in resolved-particle simulations of fluidized beds, *Phys. Rev. Fluids* **2**, 114305 (2017).
- [22] D. P. Willen and A. Prosperetti, Resolved simulations of sedimenting suspensions of spheres, *Phys. Rev. Fluids* **4**, 014304 (2019).
- [23] E. Brown and G. Ahlers, Rotations and cessations of the large-scale circulation in turbulent Rayleigh-Bénard convection, *J. Fluid Mech.* **568**, 351 (2006).
- [24] C. Morize, E. Herbert, and A. Sauret, Resuspension threshold of a granular bed by localized heating, *Physical Review E* **96**, 032903 (2017).

- [25] C. Sturtz, É. Kaminski, A. Limare, and S. Tait, The fate of particles in a volumetrically heated convective fluid at high Prandtl number, *J. Fluid Mech.* **929**, A28 (2021).
- [26] G. Lavorel and M. Le Bars, Sedimentation of particles in a vigorously convecting fluid, *Phys. Rev. E* **80**, 046324 (2009).
- [27] R. J. Munro, N. Bethke, and S. B. Dalziel, Sediment resuspension and erosion by vortex rings, *Phys. Fluids* **21**, 046601 (2009).
- [28] Y. Tsuji, T. Tanaka, and T. Ishida, Lagrangian numerical simulation of plug flow of cohesionless particles in a horizontal pipe, *Powder Technol.* **71**, 239 (1992).
- [29] G. Barnocky and R. H. Davis, Elastohydrodynamic collision and rebound of spheres: experimental verification, *Phys. Fluids* **31**, 1324 (1988).
- [30] C. T. Crowe, J. D. Schwarzkopf, M. Sommerfeld, and Y. Tsuji, *Multiphase Flows with Droplets and Particle*, 2nd ed. (Boca Raton FL: CRC Press, 2012).
- [31] J. Sun and M. M. Chen, A theoretical analysis of heat transfer due to particle impact, *Int. J. Heat Mass Transfer* **31**, 969 (1988).
- [32] R. H. Davis, J.-M. Serayssol, and E. J. Hinch, The elastohydrodynamic collision of two spheres, *J. Fluid Mech.* **163**, 479 (1986).